Rare Met. (2021) 40(5):1239–1246
https://doi.org/10.1007/s12598-020-01644-6

RARE METALS

ORIGINAL ARTICLE

Zr–Ti–Al–Fe–Cu bulk metallic glasses for biomedical device application

Kai-Ming Han, Hui Jiang*, Ying-Min Wang*, Jian-Bing Qiang

Received: 22 March 2020 / Revised: 26 April 2020 / Accepted: 2 November 2020 / Published online: 7 January 2021

Abstract A series of $Zr_{63.5-x}Ti_xAl_9Fe_{4.5}Cu_{23}$ (x = 0, 1.5, 3.0, 4.5, 6.0; at%) bulk metallic glasses (BMGs) were designed and produced by means of copper mold suction casting. The effect of Ti addition on the glass-forming ability (GFA) and mechanical properties of $Zr_{63.5-x}Ti_x$-$Al_9Fe_{4.5}Cu_{23}$ alloys was first investigated. The glass-forming ability and room-temperature plasticity of BMGs increase first and then reduced with Ti content increasing. At x = 3.0, the $Zr_{60.5}Ti_3Al_9Fe_{4.5}Cu_{23}$ BMG showed a critical glass formation diameter of 10 mm and excellent room-temperature compressive plasticity (ε_P = 4.7%) by using the samples with dimensions of Φ3 mm × 6 mm. Meanwhile, the BMG also showed better biocompatibility and biocorrosion resistance compared with Ti6Al4V alloy. Under the imitated human body condition, the corrosion current density (I_{corr}) of BMG was 6.61 × 10^{-10} A·cm^{-2}, which is two orders of magnitude lower than that of conventional Ti6Al4V alloy. Moreover, the CCD-986sk cell viabilities are, respectively, 65.4% and 46.6% on the BMG and Ti6Al4V alloy, indicating better biocompatibility of BMG. The $Zr_{60.5}Ti_3Al_9Fe_{4.5}Cu_{23}$ BMG with larger GFA, excellent mechanical properties, biocompatibility and biocorrosion resistance is considered as a potential material in biomedical device fields.

K.-M. Han, H. Jiang*
College of Mechanical and Electronic Engineering, Shandong University of Science and Technology, Qingdao 266590, China
e-mail: Jianghui2019@sdust.edu.cn

Y.-M. Wang*, J.-B. Qiang
Key Laboratory of Materials Modification (Ministry of Education), Dalian University of Technology, Dalian 116024, China
e-mail: apwangym@dlut.edu.cn

Keywords Bulk metallic glasses; Biomedical material; Mechanical property; Biocompatibility

1 Introduction

In recent years, with the aggravation of population aging and the increase in mechanical injury, the market demands of metallic biomaterials keep increasing. Owing to higher specific strength, excellent corrosion resistance and better bone integration, the titanium and the titanium alloy are currently the most widely used biomaterials, especially for Ti6Al4V alloy [1, 2]. However, the release of vanadium ions to human body in clinic makes it difficult to guarantee the biological safety of the Ti6Al4V alloy [3]. At the same time, the stress-shielding effect caused by high elastic modulus and the granular disease induced by wear products are also crucial issues [1, 4]. Therefore, the new metallic materials with property combination of lower elastic modulus, ultrahigh strength and better biocompatibility can be ideal biomaterials.

Compared with other BMGs as biomedical materials [5, 6], because of property combination of high glass-forming ability (GFA), ultrahigh strength and better biocompatibility, Zr-based bulk metallic glasses (BMGs) are favorable and potential biomedical materials, especially as surgical devices like blades and minimally invasive components [7–10]. BMG alloys with large GFAs are vital for the processing of medical materials. So far, there are many multi-component alloy systems in Zr-based BMGs with a centimeter-sized critical glass formation diameter (d_{max}), such as Zr–Ti–Ni–Cu–Be [11], Zr–Al–Ni–Cu [12], Zr–Al–Fe–Cu [13], Zr–Al–Ag–Cu [14] and Zr–Al–Co [15, 16], while most of them contain toxic or precious metal

elements like Be, Ag and Ni, which are adverse for biomedical alloys. Recently, many non-toxic (Ni and Be free) and cheap (Pd free) Zr–Al–Fe–Cu BMGs with exceptionally high glass-forming abilities were fabricated as biomedical materials [13, 17–20]. For example, $Zr_{58}Al_{12}Fe_8Cu_{22}$ BMG with a critical casting diameter of 13 mm was first reported in Zr–Al–Fe–Cu system by Jin and Löffler [13]. $Zr_{60}Al_{10}Fe_5Cu_{25}$ and $Zr_{62.5}Al_{10}Fe_5Cu_{22.5}$ BMG alloys with a critical casting diameter of 20 mm were easily synthesized by Inoue et al. [17]. Nevertheless, these BMGs with superior high glass-forming abilities generally exhibit limited room-temperature plasticity, which has led to their restricted use as biomedical materials. Hence, synthesizing cheap and non-toxic Zr-based BMGs with large glass formation abilities and better room-temperature plasticity is of great importance for the biomedical device applications.

In our previous work, $Zr_{63.5}Al_9Fe_{4.5}Cu_{23}$ BMG (d_{max} = 10 mm) was designed by a dual-cluster formulism and produced with by means of using the high-purity raw materials [21]. As a typical biomedical alloying element, Ti was widely used as various bioimplants. However, effects of Ti addition on glass-forming ability, thermal glass stability and mechanical properties of the Zr–Al–Fe–Cu BMGs were quite indistinct [22], especially for BMGs produced by low-cost raw materials. Hence, a series of $Zr_{63.5-x}Ti_xAl_9Fe_{4.5}Cu_{23}$ (x = 0, 1.5, 3.0, 4.5, 6.0; at%) alloys were designed and produced with sponge zirconium and other industrial raw materials to reduce the production costs and further improve the glass-forming ability, mechanical properties and biocompatibility of the basic alloy.

2 Experimental

2.1 Materials preparation and characterization

Master ingots with nominal compositions of $Zr_{63.5-x}Ti_xAl_9Fe_{4.5}Cu_{23}$ (x = 0, 1.5, 3.0, 4.5, 6.0; at%) were prepared by arc melting low-cost sponge zirconium (Zr + Hf > 99.4 wt%), industrial aluminum, iron, copper and titanium metals (> 99.5 wt%). During the melting process, the Ti ingot was first melted for oxygen content control. Meanwhile, to ensure the compositional homogeneity, every alloy ingot was carefully remelted four or five times. All rod samples were prepared by the copper mold suction casting and ribbon samples were made by the melt spinning method. Microstructures of as-cast rod and ribbon samples were first characterized by X-ray diffraction (XRD, Bruker D8 Focus, Cu Kα). And to ensure the nature of amorphous structure of BMGs, transmission electron microscope (TEM, TECNAI G20) was also used. The thermal behaviors of ribbon samples were performed by using differential scanning calorimetry (DSC, TA Q100) at a constant heating rate of 40 K·min^{-1} and differential thermal analysis (DTA, TA Q600) at the heating rate of 20 K·min^{-1}. To evaluate the mechanical properties of as-cast BMG alloys under compression, specimens with a size of Φ3 mm × 6 mm were fabricated and tested using a material testing system (MTS, Landmark 250 kN) at a strain rate of 5×10^{-4} s^{-1}. The fracture surface morphologies of the alloy samples were observed by scanning electron microscope (SEM, Zeiss supra 55). In order to ensure the accuracy, at least 3 samples with same composition were tested.

2.2 Cell cytotoxicity and morphological observation

The human fibroblast cell line CCD-986sk was adopted to evaluate the cell cytotoxicity of Zr-based BMGs and Ti6Al4V alloy. BMG samples were first polished and sterilized via ultraviolet radiation and placed in 96-well plates. Then, the CCD-986sk cells with a density of 0.5×10^4 cells·well^{-1} in the 96-well plates were cultured in Dulbecco's modified Eagle's medium (DMEM) supplemented with 10% fetal bovine serum (FBS) in a 5% CO_2 balanced incubator at 37 °C. After 24-h incubation, MTS solution (20 μl) was added to each well in the culture plate, which was then placed in 5% CO_2/95% air environment with a constant temperature of 37 °C for 30 min to make it fully react. Afterward, 150 μl formazan solubilization solution (DMSO) was added to the MTS solution and gently shaken for 10 min. Finally, spectrophotometric absorbance measurements were tested by using a microplate reader at 490 nm. To reduce experiment error, six specimens of the same composition were tested under the same condition. Meanwhile, six blank tests were performed for comparison. According to the same experimental process [23], the cell morphologies on BMG and Ti6Al4V samples were observed by SEM.

2.3 Biocorrosion examinations

To evaluate the biocorrosion behaviors of Zr-based BMGs and Ti6Al4V alloy in the imitated human body (phosphate-buffered solution, PBS), electrochemical polarization measurements at a constant temperature of 37 °C were carried out by a three-electrode system. After at least 10-min immersion, the open-circuit potentials (OCP) almost became stable. Then, potentiodynamic polarization curves were performed at a constant rate of 1 mV·s^{-1}. Besides, immersion tests of Zr-based BMGs and Ti6Al4V alloy with a dimension of Φ3 mm × 1 mm were conducted in PBS for 30 days at 37 °C. After immersion tests, the sample morphologies were also observed by SEM.

3 Results and discussion

3.1 Glass formation characterization

XRD patterns of as-cast $Zr_{63.5-x}Ti_xAl_9Fe_{4.5}Cu_{23}$ (x = 0, 1.5, 3.0, 4.5, 6.0; at%) rod samples with a diameter varying from 3 to 10 mm are presented in Fig. 1a. It can be observed that all rod samples show no crystalline diffraction peaks, which indicates all alloy samples with different diameters are amorphous in nature. The critical glass formation diameters of BMGs are shown in Fig. 1a. As the basic composition, $Zr_{63.5}Al_9Fe_{4.5}Cu_{23}$ (x = 0) alloy shows a critical glass formation size of 6 mm. With Ti content increasing from x = 0 to x = 3.0, the corresponding value of d_{max} is changed from 6 to 10 mm. Nevertheless, with Ti content further increasing, the glass formation d_{max} will significantly decrease to 3 mm at x = 6.0. It can be observed that, with the increase in Ti content, the GFAs of $Zr_{63.5-x}Ti_xAl_9Fe_{4.5}Cu_{23}$ BMG alloys exhibit a tendency of increasing first and then decreasing later. Among the BMG alloys, $Zr_{60.5}Ti_3Al_9Fe_{4.5}Cu_{23}$ alloy shows the largest GFA (d_{max} = 10 mm) at x = 3.0. The high-resolution transmission electron microscopy (HRTEM) image of $Zr_{60.5}Ti_3Al_9Fe_{4.5}Cu_{23}$ BMG with 10 mm in diameter is shown in Fig. 1b. From the image, any periodically ordered feature is not observed and there is only a homogeneous contrast. Meanwhile, as shown in the inset in Fig. 1b, the corresponding selected area electron diffraction (SAED) patterns with typical diffuse halo rings also show the nature of an amorphous structure. The above results indicate that d_{max} of $Zr_{60.5}Ti_3Al_9Fe_{4.5}Cu_{23}$ BMG alloy can reach centimeter scale by the conventional copper mold suction casting method.

$Zr_{63.5}Al_9Fe_{4.5}Cu_{23}$ BMG shows a glass formation d_{max} of 10 mm when prepared with high-purity raw materials in high vacuum casting conditions. However, with low-cost raw materials in low vacuum, the critical glass formation size of $Zr_{63.5}Al_9Fe_{4.5}Cu_{23}$ BMG was only 6 mm. This shows that oxygen and other impurities in raw materials or low vacuum casting condition have obviously influenced the GFAs of Zr-based BMGs. The oxygen and other impurities generally result in heterogeneous nucleation during the solidification and reduce glass formation abilities of BMG alloys [24]. At the same time, it is considered that using low-cost raw materials in low vacuum casting condition to prepare Zr-based BMGs with superior GFA is quite difficult. In the present work, by adding appropriate Ti content, the GFA of the basic alloy is obviously improved. And the glass formation d_{max} of $Zr_{60.5}Ti_3Al_9Fe_{4.5}Cu_{23}$ BMG alloy is up to 10 mm. This may be attributed to the fact that adding appropriate Ti in the basic alloy restrains the aggregation of oxygen and impurities as the catalytic sites of heterogeneous nucleation, which improves the glass formation abilities of basic alloy. On the other hand, according to the "confusion principle" [25], the addition of Ti in liquid alloys reduces the probability of forming a special crystal structure, which is favorable to the glass formation of alloys.

3.2 Thermal characterization

Figure 2a, b, respectively, shows DSC and DTA curves of the $Zr_{63.5-x}Ti_xAl_9Fe_{4.5}Cu_{23}$ BMG samples in the heating process. It can be seen in Fig. 2a that all of the BMG samples show an obvious glass transition, followed by a supercooled liquid region before crystallization. As shown in Fig. 2a, the glass transition temperature (T_g) and the onset crystallization temperature (T_x) are marked by arrows. T_g ($\sim$ 660 K) almost keeps constant with the increase in Ti content. Moreover, with the increase in Ti

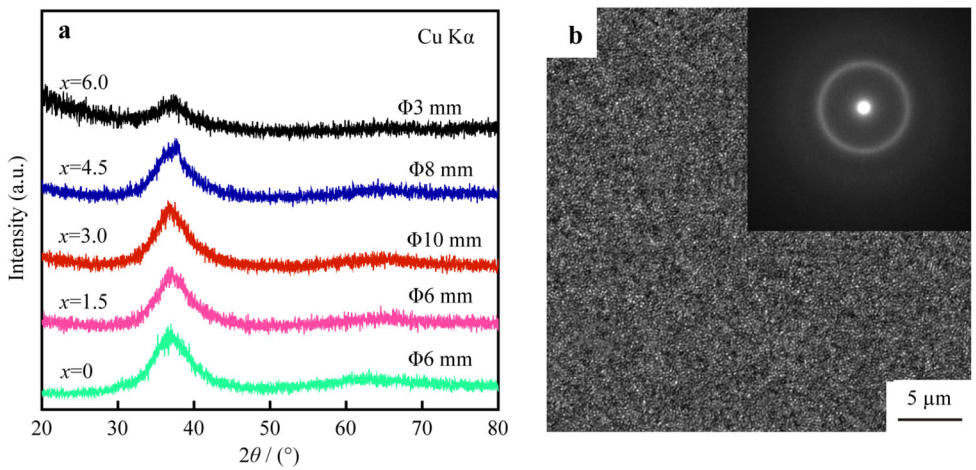

Fig.1 **a** XRD patterns of $Zr_{63.5-x}Ti_xAl_9Fe_{4.5}Cu_{23}$ (x = 0, 1.5, 3.0, 4.5, 6.0; at%) BMG rod samples; **b** HRTEM image and SAED pattern (inset) of $Zr_{60.5}Ti_3Al_9Fe_{4.5}Cu_{23}$ BMG with 10 mm in diameter

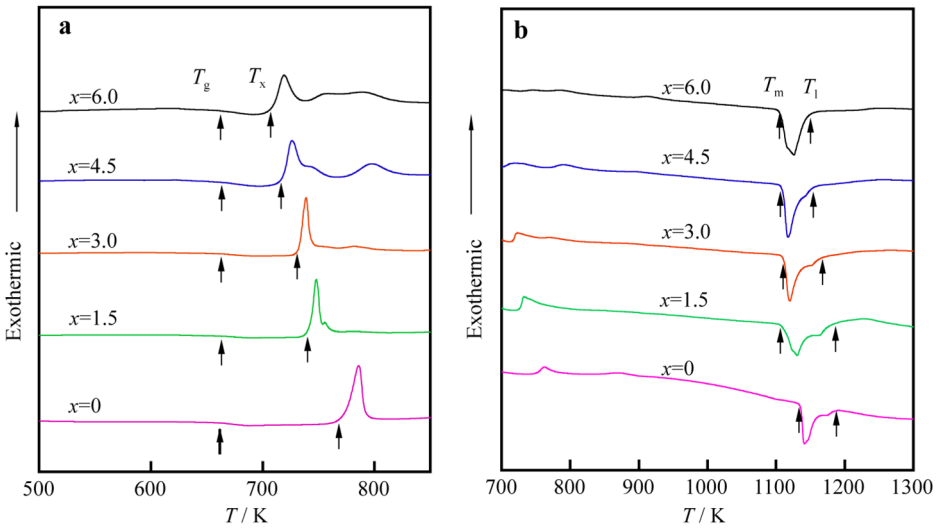

Fig. 2 **a** DSC and **b** DTA curves measured from $Zr_{63.5-x}Ti_xAl_9Fe_{4.5}Cu_{23}$ (x = 0, 1.5, 3.0, 4.5, 6.0; at%) ribbon samples

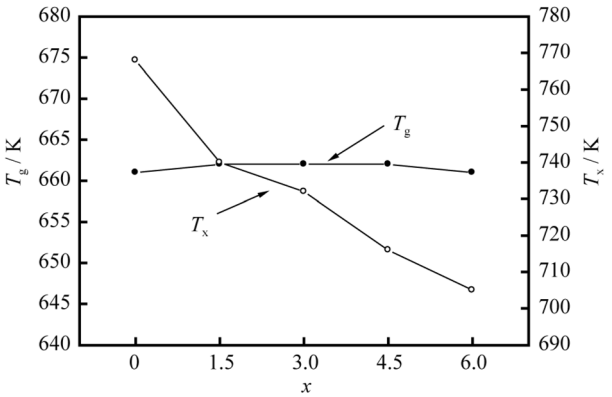

Fig. 3 T_g and T_x vs. x in $Zr_{63.5-x}Ti_xAl_9Fe_{4.5}Cu_{23}$ (x = 0, 1.5, 3.0, 4.5, 6.0; at%) BMGs

content, T_x shows a decreasing trend from 768 K (x = 0) to 705 K (x = 6.0). Therefore, the supercooled liquid span ($\Delta T_x = T_x - T_g$ [26]) shows a reducing trend from 110 K (x = 0) to 44 K (x = 6.0).

The variation tendency of T_g and T_x is summarized in Fig. 3. With the further increase in temperature, these BMG samples begin to melt. From the DTA curves (Fig. 2b), it can be seen that DTA curves of these BMG alloys consist of one principal melting peak, followed a shallow melting step. The melting curves of Fig. 2b show that the onset melting temperature (T_m) decreases from 1135 K (x = 0) to 1105 K (x = 6.0) with Ti content increasing. Similarly, the liquidus temperature (T_l) decreases from 1186 K (x = 0) to 1149 K (x = 6.0). The reduced glass temperature ($T_{rg} = T_g/T_l$ [27]) can be calculated. The values show an increasing trend from 0.555 (x = 0.0) to 0.575 (x = 6.0), which is inconsistent with the variation tendency of GFAs of Zr–Ti–Al–Fe–Cu BMGs. The GFA assessment by the characteristic parameter of T_{rg} is not consistent with the casting results in this BMG system. The relevant parameters of $Zr_{63.5-x}Ti_xAl_9Fe_{4.5}Cu_{23}$ BMGs are listed in Table 1.

Table 1 Parameters of glass formation and compressive properties of as-cast $Zr_{63.5-x}Ti_xAl_9Fe_{4.5}Cu_{23}$ BMG alloys

Alloys	T_g/K	T_x/K	ΔT_x/K	T_m/K	T_l/K	T_{rg}/K	d_{max}/mm	σ_y/GPa	ε_p/%
x = 0	658	768	110	1135	1186	0.555	6	1.58	1.6
x = 1.5	662	740	78	1108	1185	0.559	6	1.58	2.5
x = 3.0	662	732	70	1112	1165	0.568	10	1.63	4.7
x = 4.5	662	716	54	1107	1153	0.574	8	1.66	3.8
x = 6.0	661	705	44	1105	1149	0.575	3	1.69	0.9

T_g—glass transition temperature; T_x—onset crystallization temperature; ΔT_x—supercooled liquid span; T_m—onset melting temperature; T_l—liquidus temperature; T_{rg}—reduced glass temperature; d_{max}—critical glass formation diameter; σ_y—compressive strength; ε_p—compressive plastic strain

3.3 Mechanical characteristics

Figure 4 presents the engineering compressive stress–strain curves of $Zr_{63.5-x}Ti_xAl_9Fe_{4.5}Cu_{23}$ BMG alloys. It is noticed that BMG samples with a size of Φ3 mm × 6 mm are tested to obtain accurate experimental results. From the compressive curves, it can be seen that all alloy samples show different plastic strain depending on the BMG composition. As the Ti content increases, the compressive strength (σ_y) increases slightly from 1.58 GPa (x = 0) to 1.69 GPa (x = 6.0). The compressive plastic strain (ε_P) first increases from 1.6% (x = 0) to 4.7% (x = 3.0), and then decreases to 0.9% (x = 6.0). The relevant mechanical property parameters such as σ_y and ε_P are listed in Table 1. Many serrations on the stress–strain curves were observed. The serration behavior is related to avalanches of deformation processes [28]. Once the stress in the BMGs reaches a critical value, the shear band on the surface of the samples will be initiated and propagate, resulting in abrupt deformation.

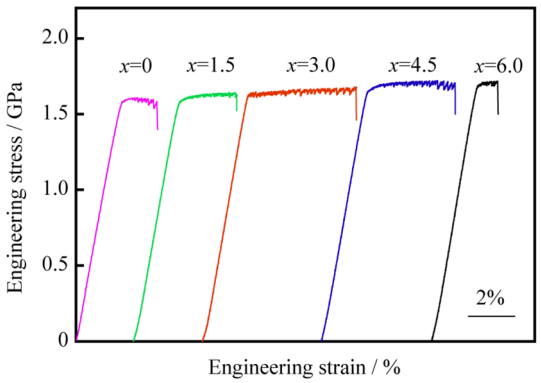

Fig. 4 Compressive stress–strain curves of $Zr_{63.5-x}Ti_xAl_9Fe_{4.5}Cu_{23}$ (x = 0.0, 1.5, 3.0, 4.5, 6.0; at%) BMG samples

Figure 5 presents the fracture surface morphologies of $Zr_{63.5-x}Ti_xAl_9Fe_{4.5}Cu_{23}$ (x = 0 and 3.0) BMGs after fracture. As shown in Fig. 5a, b, vein pattern forms on the fracture surface of $Zr_{63.5}Al_9Fe_{4.5}Cu_{23}$ alloy, which is a typical feature of BMG alloys after fracture [29]. The formation of vein pattern is mainly caused by the local melting in the shear bands, resulting from the instantaneous release of high elastic energy. The post-melting feature of vein pattern is marked by the arrow in Fig. 5a, b. However, $Zr_{60.5}Ti_3Al_9Fe_{4.5}Cu_{23}$ BMG with improved room-temperature plasticity shows a unique fracture morphology, as

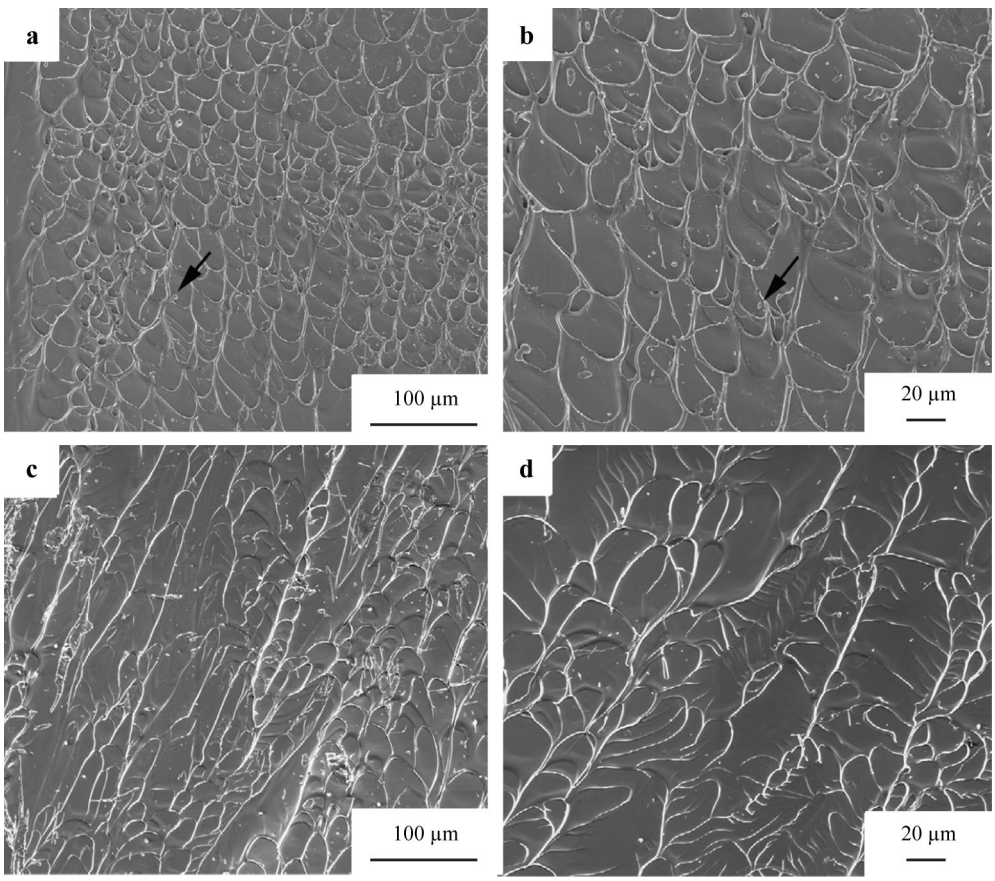

Fig. 5 SEM images of fracture surface of **a, b** $Zr_{63.5}Al_9Fe_{4.5}Cu_{23}$ and **c, d** $Zr_{60.5}Ti_3Al_9Fe_{4.5}Cu_{23}$ BMG alloys

shown in Fig. 5c, d. In addition to the typical vein pattern, there are a large number of fish bone patterns in the fracture surface. These fish bone patterns are evenly distributed between the vein pattern. The backbone parts of the fish bone pattern are arranged along the shear direction, and the regular bone thorns are distributed on both sides of the trunk. Similar fracture morphology has been reported in other Zr-based BMGs with good room-temperature plasticity [30, 31]. This pattern may be ascribed to form by the stable release of high elastic energy accompanied by the slow crack propagation rate [32].

Significantly, $Zr_{60.5}Ti_3Al_9Fe_{4.5}Cu_{23}$ alloy with the largest GFA shows the excellent plasticity in the alloy system. Room-temperature plasticity of about 4.7% is obtained by using the samples with dimensions of Φ3 mm × 6 mm. It is recognized that a larger sample size usually produces a lower room-temperature plasticity. Therefore, the above results indicate that the room-temperature plasticity can be effectively improved by adding an appropriate amount of Ti in the present BMG system. The compressive plasticity of BMGs is related to the local structural heterogeneities [33]. It is noted that Ti–Zr atomic pair has a positive heat of mixing of 0 $kJ \cdot mol^{-1}$ [34]. Thus, with addition of Ti in the Zr–Al–Fe–Cu system, the degree of inhomogeneity of the amorphous structure may be enhanced due to this chemical affinity characteristic. On the other hand, the presence of a certain amount of oxygen and other impurities may also further increase the microstructural inhomogeneity in the melting process. As the nucleation sites, the local structural heterogeneities can result in the formation of a number of shear bands, which is beneficial to the compressive plasticity of BMGs.

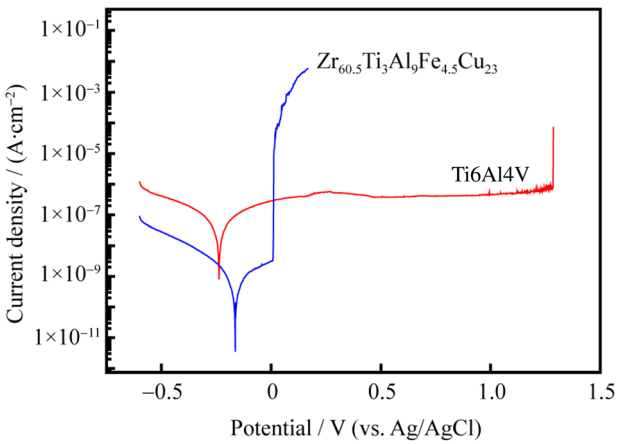

Fig. 6 Potentiodynamic polarization curves of $Zr_{60.5}Ti_3Al_9Fe_{4.5}Cu_{23}$ BMG and Ti6Al4V alloy in PBS at 37 °C

3.4 Corrosion resistance tests

Figure 6 presents the potentiodynamic polarization curve of $Zr_{60.5}Ti_3Al_9Fe_{4.5}Cu_{23}$ BMG in PBS open to air at 37 °C. For comparison, the potentiodynamic polarization curve of Ti6Al4V alloy under the same condition was also given. The corrosion potentials (E_{corr}) of the $Zr_{60.5}Ti_3Al_9Fe_{4.5}Cu_{23}$ BMG and Ti6Al4V alloy are, respectively, − 0.162 and − 0.238 V. Meanwhile, the corrosion current densities (I_{corr}) of the BMG is 6.61×10^{-10} $A \cdot cm^{-2}$. Compared with Ti6Al4V ($I_{corr} = 1.0 \times 10^{-8}$ $A \cdot cm^{-2}$), the value is lower, showing lower corrosion rate under the same condition. This indicates that the corrosion rate of the $Zr_{60.5}Ti_3Al_9Fe_{4.5}Cu_{23}$ BMG is superior to that of Ti6Al4V alloy in the human body fluid. The low corrosion current density can be explained according to the electronic structure features of the alloys. Compared to Ti6Al4V alloy, a typical crystalline metal, $Zr_{60.5}Ti_3Al_9Fe_{4.5}Cu_{23}$ BMG shows a high resistivity and the low electron density of states at the Fermi level. Thus, fewer electrons are available for electrochemical reaction of BMG, causing

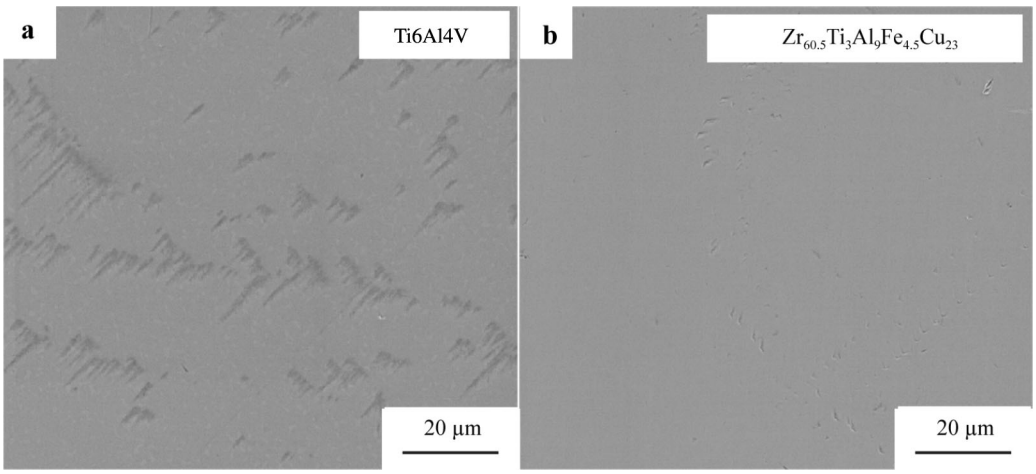

Fig. 7 SEM images of **a** Ti6Al4V alloy and **b** $Zr_{60.5}Ti_3Al_9Fe_{4.5}Cu_{23}$ BMG after 30 days immersing in PBS at 37 °C

relatively low corrosion current density. In addition, the compact passive film formed in the process of electrochemical reaction also plays an important role for the alloy [35, 36]. Figure 7 presents the surface morphologies of the $Zr_{60.5}Ti_3Al_9Fe_{4.5}Cu_{23}$ BMG and Ti6Al4V alloy at constant temperature of 37 °C after 30 days immersing in PBS. The corrosion with different degrees for the alloys can be observed. The number density of the corrosion pits in the BMG surface is clearly much less than that of Ti6Al4V alloy, which means that BMG shows the better corrosion resistance under the same condition. Therefore, $Zr_{60.5}Ti_3Al_9Fe_{4.5}Cu_{23}$ BMG is considered as a potential material in biomedical device fields.

3.5 Cytotoxicity tests

From Fig. 8, it can be seen that the CCD-986sk cell viabilities on the $Zr_{60.5}Ti_3Al_9Fe_{4.5}Cu_{23}$ BMG and Ti6Al4V alloy are, respectively, 65.4% and 46.6%. As the negative control, the cell viability of culture solution containing no metal ions is 100%. The cell viability results indicate that the BMG shows superior biocompatibility than conventional Ti6Al4V alloy under the same condition. Figure 9 presents SEM images of adhesion cell morphologies on BMG and Ti6Al4V alloy specimens after 24-h incubation. From Fig. 9, we can find that the CCD-986sk cells on Ti6Al4V alloy are relatively small and less spread out. As a comparison, those on BMG samples show a widespread morphology, which indicates that the BMG alloy is much more beneficial for cell compatibility compared to Ti6Al4V alloy. In addition, the cells on BMG show significantly longer structures of fibrillar adhesion compared to those on Ti6Al4V alloy, indicating superior cell adhesion.

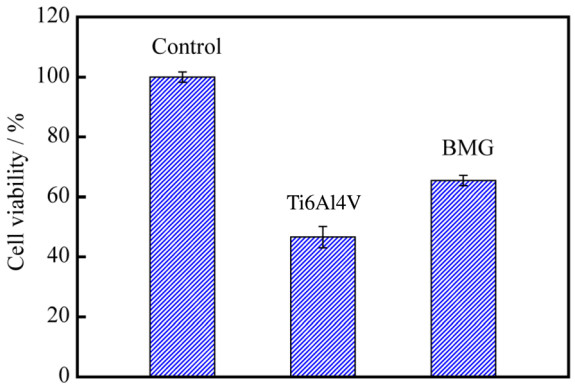

Fig. 8 CCD-986sk cell viability on $Zr_{60.5}Ti_3Al_9Fe_{4.5}Cu_{23}$ BMG and Ti6Al4V alloy after 24-h incubation

4 Conclusion

In the present work, a series of $Zr_{63.5-x}Ti_xAl_9Fe_{4.5}Cu_{23}$ (x = 0−6.0) BMGs were successively designed and fabricated. The results suggested that the glass-forming abilities and mechanical properties of $Zr_{63.5-x}Ti_xAl_9Fe_{4.5}Cu_{23}$ BMGs can be enhanced by adding an appropriate amount of Ti. The $Zr_{60.5}Ti_3Al_9Fe_{4.5}Cu_{23}$ (x = 3.0) BMG showed the highest glass-forming ability (d_{max} = 10 mm) as well as room-temperature compressive plasticity (ε_p = 4.7%). This may be attributed to the alloying effect of Ti which aggravates the structural heterogeneities in the amorphous alloys due in part to the positive heat of mixing between Ti and Zr. In addition, the BMG shows excellent biocorrosion resistance, and its passive current density is two orders of magnitude lower than that of Ti6Al4V alloy. The cell viability of 65.4% on BMG is obviously superior to that on Ti6Al4V alloy (46.6%), demonstrating good biocompatibility. These results indicate that $Zr_{60.5}Ti_3Al_9Fe_{4.5}Cu_{23}$ BMG shows considerable potential for biomedical device applications.

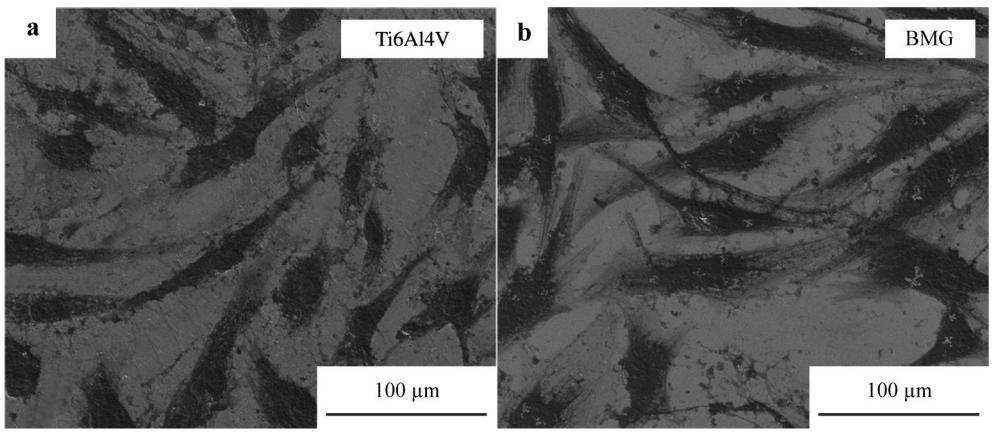

Fig. 9 SEM images of CCD-986sk cells adhesion on **a** Ti6Al4V alloy and **b** $Zr_{60.5}Ti_3Al_9Fe_{4.5}Cu_{23}$ BMG

Acknowledgements This work was supported by the National Natural Science Foundation of China (Nos. 51901116 and 51671045), the Science Challenge Project (No. TZ2016004), the Fundamental Research Funds for the Central Universities (Nos. DUT16ZD209 and DUT18GF112) and the National Magnetic-Confinement Fusion Science Program (Nos. 2013GB107003 and 2015GB105003).

References

[1] Geetha M, Singh AK, Asokamani R, Gogia AK. Ti based biomaterials, the ultimate choice for orthopaedic implants—a review. Prog Mater Sci. 2009;54(3):397.
[2] Zhang LC, Chen LY. A review on biomedical titanium alloys: recent progress and prospect. Adv Eng Mater. 2019;21(4): 1801215.
[3] Costa BC, Tokuhara CK, Rocha LA, Oliveira RC, Lisboa-Filho PN, Pessoa JC. Vanadium ionic species from degradation of Ti–6Al–4V metallic implants: in vitro cytotoxicity and speciation evaluation. Mater Sci Eng C Mater Biol Appl. 2019;96:730.
[4] Long M, Rack H. Titanium alloys in total joint replacement—a materials science perspective. Biomaterials. 1998;19(18):1621.
[5] Yan HM, Liu Y, Pang SJ, Zhang T. Glass formation and properties of Ti-based bulk metallic glasses as potential biomaterials with Nb additions. Rare Met. 2018;37(10):831.
[6] Liu Y, Wang HJ, Pang SJ, Zhang T. Ti–Zr–Cu–Fe–Sn–Si–Ag–Ta bulk metallic glasses with good corrosion resistance as potential biomaterials. Rare Met. 2020;39(6):688.
[7] Han KM, Qiang JB, Wang YM, Zhao BB, Häussler P. $Zr_{55.8}Al_{19.4}(Co_{1-x}Cu_x)_{24.8}$ (x = 0–0.8 at%) bulk metallic glasses for surgical devices applications. J Iron Steel Res Int. 2018;25(6):644.
[8] Han KM, Qiang JB, Wang YM, Häussler P. Zr–Al–Co–Cu bulk metallic glasses for biomedical devices applications. J Alloy Compd. 2017;729:144.
[9] Li HF, Zheng YF. Recent advances in bulk metallic glasses for biomedical applications. Acta Biomater. 2016;36:1.
[10] Tsai PH, Lin YZ, Li JB, Jian SR, Jang JSC, Li C, Chu JP, Huang JC. Sharpness improvement of surgical blade by means of ZrCuAlAgSi metallic glass and metallic glass thin film coating. Intermetallics. 2012;31:127.
[11] Peker A, Johnson WL. A highly processable metallic glass: $Zr_{41.2}Ti_{13.8}Cu_{12.5}Ni_{10.0}Be_{22.5}$. Appl Phys Lett. 1993;63(17):2342.
[12] Inoue A, Zhang T. Fabrication of bulk glassy $Zr_{55}Al_{10}Ni_5Cu_{30}$ alloy of 30 mm in diameter by a suction casting method. Mater Trans JIM. 1996;37(2):185.
[13] Jin K, Löffler JF. Bulk metallic glass formation in Zr–Cu–Fe–Al alloys. Appl Phys Lett. 2005;86(24):241909.
[14] Zhang QS, Zhang W, Inoue A. Preparation of $Cu_{36}Zr_{48}Ag_8Al_8$ bulk metallic glass with a diameter of 25 mm by copper mold casting. Mater Trans. 2007;48(3):629.
[15] Wada T, Qin FX, Wang XM, Yoshimura M, Inoue A, Sugiyama N, Ito R, Matsushita N. Formation and bioactivation of Zr–Al–Co bulk metallic glasses. J Mater Res. 2011;24(09):2941.
[16] Inoue A, Takeuchi A. Recent development and application products of bulk glassy alloys. Acta Mater. 2011;59(6):2243.
[17] Zhang QS, Zhang W, Inoue A. Ni-free Zr–Fe–Al–Cu bulk metallic glasses with high glass-forming ability. Scripta Mater. 2009;61(3):241.
[18] Monfared A, Vali H, Faghihi S. Biocorrosion and biocompatibility of Zr–Cu–Fe–Al bulk metallic glasses. Surf Interface Anal. 2013;45(11–12):1714.
[19] Yu DC, Shi XG, Fu HM, Geng Y, Zhu ZW, Qi Y, Zhang HF. Glass formation in Zr–Al–Fe–Cu system. Mater Lett. 2015;157: 299.
[20] Wang SS, Wang YL, Wu YD, Wang T, Hui XD. High plastic Zr–Cu–Fe–Al–Nb bulk metallic glasses for biomedical applications. Int J Miner Metall Mater. 2015;22(6):648.
[21] Han KM, Wang YM, Qiang JB, Zhang HB, Qin SX, Jiang H, Zhang S, Dong C. Dual-cluster formulas for eutectic-type bulk metallic glasses and experimental verification in Zr–Al–Fe–Cu system. Mater Des. 2019;183:108142.
[22] Shi HQ, Zhao WB, Wei XW, Ding Y, Shen XD, Liu WJ. Effect of Ti addition on mechanical properties and corrosion resistance of Ni-free Zr-based bulk metallic glasses for potential biomedical applications. J Alloy Compd. 2020;815:152636.
[23] Han KM, Wang YM, Qiang JB, Jiang H, Gu LW. Low-cost Zr-based bulk metallic glasses for biomedical devices applications. J Non-Cryst Solids. 2019;520:119442.
[24] Pajor K, Kozieł T, Cios G, Błyskun P, Bała P, Zielińska-Lipiec A. Glass forming ability of the $Zr_{50}Cu_{40}Al_{10}$ alloy with two oxygen levels. J Non-Cryst Solids. 2018;496:42.
[25] Greer AL. Confusion by design. Nature. 1993;366(6453):303.
[26] Inoue A. Stabilization of metallic supercooled liquid and bulk amorphous alloys. Acta Mater. 2000;48(1):279.
[27] Turnbull D. Under what conditions can a glass be formed? Contemp Phys. 1969;10(5):473.
[28] Zhang Y, Liu JP, Chen SY, Xie X, Liaw PK, Dahmen KA, Qiao JW, Wang YL. Serration and noise behaviors in materials. Prog Mater Sci. 2017;90:358.
[29] Trexler MM, Thadhani NN. Mechanical properties of bulk metallic glasses. Prog Mater Sci. 2010;55(8):759.
[30] Deng XD, Chen SS, Hu Q, Xie SH, Zou JZ, Sial MAZG, Zeng XR. Excellent room-temperature mechanical properties in the high glass- forming Zr–Cu–Ni–Al–Nb alloy system. Mater Res Express. 2019;6(8):086551.
[31] Cao GH, Liu K, Liu GP, Zong HT, Bala H, Zhang BQ. Improving the glass-forming ability and the plasticity of Zr–Cu–Al bulk metallic glass by addition of Nb. J Non-Cryst Solids. 2019;513:105.
[32] Sun BA, Tan J, Pauly S, Kühn U, Eckert J. Stable fracture of a malleable Zr-based bulk metallic glass. J Appl Phys. 2012; 112(10):103533.
[33] Qiao JC, Wang Q, Pelletier JM, Kato H, Casalini R, Crespo D, Pineda E, Yao Y, Yang Y. Structural heterogeneities and mechanical behavior of amorphous alloys. Prog Mater Sci. 2019;104:250.
[34] Takeuchi A, Inoue A. Classification of bulk metallic glasses by atomic size difference, heat of mixing and period of constituent elements and its application to characterization of the main alloying element. Mater Trans. 2005;46(12):2817.
[35] Wu YM, Zhang CZ, Qiu PY, Li ZC, Li HP, Wang CM. Effect of Ti substitution on the hardness and electrochemical property of laser clad Zr–Al–Co (Ti) amorphous-nanocrystalline coating. Mater Res Express. 2018;6(2):026506.
[36] Zhang CZ, Qiu NN, Kong LL, Yang XD, Li HP. Thermodynamic and structural basis for electrochemical response of Cu–Zr based metallic glass. J Alloy Compd. 2015;645:487.